Effects of Frequency, Permittivity, and Voxel Size on Predicted Specific Absorption Rate Values in Biological Tissue During Electromagnetic-Field Exposure

Patrick A. Mason, William D. Hurt, *Senior Member, IEEE*, Thomas J. Walters, John A. D'Andrea, *Member, IEEE*, Peter Gajšek, Kathy L. Ryan, David A. Nelson, Kristen I. Smith, and John M. Ziriax

***Abstract*—Current electromagnetic-field (EMF) exposure limits have been based, in part, on the amount of energy absorbed by the whole body. However, it is known that energy is absorbed nonuniformly during EMF exposure. The development and widespread use of sophisticated three-dimensional anatomical models to calculate specific-absorption-rate (SAR) values in biological material has resulted in the need to understand how model parameters affect predicted SAR values. This paper demonstrate the effects of manipulating frequency, permittivity values, and voxel size on SAR values calculated by a finite-difference time-domain program in digital homogenous sphere models and heterogeneous models of rat and man. The predicted SAR values are compared to empirical data from infrared thermography and implanted temperature probes.**

***Index Terms*—Computer modeling, conductivity, dielectric values, dosimetry, finite difference time domain, radio-frequency radiation.**

I. Introduction

PRIOR TO THE use of computer-based heterogeneous models and relatively powerful computers, the location and amount of energy absorbed during electromagnetic-field (EMF) exposure were predicted using several other techniques. For example, empirically based estimates of the whole-body specific-absorption-rate (SAR) value are commonly performed using Dewar flask or twin-well calorimetry [1], [2]. Localized SAR values can be determined using temperature changes measured by implanted thermal probes. SAR values could be extrapolated from these temperature changes using [3, Eq. 7.7], which is based on the specific heat of the tissue. Surface SAR can be determined using the same principle with infrared thermography [4]. Finally, theoretically based estimates of whole-body average SAR values have been obtained using computer-modeling techniques that utilized animals and human models constructed from prolate spheroids and cylinders [3].

During the last several years, more sophisticated computer-based models of animals and humans have been developed. Their complexity ranges from the simple homogeneous structure to the complex heterogeneous structure having small voxel sizes ($\leq$ 1 mm^3) and coded for numerous tissue types [5]–[10]. Each of these tissue types in such models is assigned a permittivity value based on the frequency-of-interest. For some tissue types, however, a range of permittivity values have been reported [11]. This range may be due to a variety of reasons, including the species origin of the tissue or difficulties in sample preparation (e.g., inflated lung).

In this paper, we determine the influence of permittivity values, frequency, and voxel size on predicted whole-body and localized SAR values in computer-based heterogeneous models of the rat and man. These results were then compared to empirical measurements in the rat to determine the validity of the models.

II. Methods

Computer-generated spheres were developed with the following characteristics: 20, 66, or 105 mm in diameter and each 1-mm cubed voxel within the sphere was assigned a dielectric value corresponding to 2/3 of that for muscle [3]. The 20-mm-diameter sphere was used for comparison of results predicted by the finite-difference time-domain (FDTD) code and Mie theory. Data from the 66- and 105-mm-diameter spheres were compared to those obtained from empirical measurements as described below in Section II-A.

Manuscript received November 12, 1999; revised April 18, 2000. This work was supported in part by U.S. Air Force Contract F41624-96-C-9009 and under Work Unit 61153N MRO4101.001 1606. The work of W. D. Hurt was supported in part by an Air Force Office of Scientific Research Award. The work of J. A. D'Andrea was supported in part by the Office of Naval Research.

P. A. Mason is with the Directed Energy Bioeffects Division, Air Force Research Laboratory, Brooks Air Force Base, TX 78235 USA and also with Conceptual MindWorks Inc., San Antonio, TX 78228 USA.

W. D. Hurt is with the Directed Energy Bioeffects Division, Air Force Research Laboratory, Brooks Air Force Base, TX 78235 USA.

T. J. Walters is with the Directed Energy Bioeffects Division, Air Force Research Laboratory, Brooks Air Force Base, TX 78235 USA and also with Veridian Engineering Inc., San Antonio, TX 78216 USA.

J. A. D'Andrea and J. M. Ziriax are with the Naval Health Research Center Detachment, Brooks Air Force Base, TX 78235 USA.

P. Gajšek is with the Directed Energy Bioeffects Division, Air Force Research Laboratory, Brooks Air Force Base, TX 78235 USA, with the Department of Biology, Trinity University, San Antonio, TX 78212 USA, and also with the Institute of Public Health of the Republic of Slovenia, Ljubljana, Slovenia.

K. L. Ryan is with the Directed Energy Bioeffects Division, Air Force Research Laboratory, Brooks Air Force Base, TX 78235 USA and also with the Department of Biology, Trinity University, San Antonio, TX 78212 USA.

D. A. Nelson is with the Center for Biomedical Engineering, Michigan Technological University, Houghton, MI 49931 USA.

K. I. Smith is with the University of Texas Health Science Center at San Antonio, San Antonio, TX 78284 USA.

Publisher Item Identifier S 0018-9480(00)09696-4.

0018–9480/00$10.00 © 2000 IEEE

TABLE I
TISSUE TYPES AND MASS DENSITY (g/cm^3) VALUES USED IN THE RAT AND/OR MAN MODELS

TISSUE	MASS DENSITY (g/cm^3)
Bile	1.01
Bladder	1.03
Blood	1.06
Blood Vessel	1.04
Body Fluid	1.01
Bone (Cancellous)	1.92
Bone (Cortical)	1.99
Bone Marrow	1.04
Brain (White Matter)	1.04
Brain (Gray Matter)	1.04
Brain (Cerebellum)	1.04
Cartilage	1.10
Cerebral Spinal Fluid	1.01
Eye (Cornea)	1.08
Eye (Lens)	1.05
Eye (Sclera/Wall)	1.03
Eye (Humor)	1.01
Fat	0.92
Gall Bladder	1.03
Gland	1.05
Heart	1.03
Intestine (Large)	1.04
Intestine (Small)	1.04
Kidney	1.05
Ligament	1.22
Liver	1.03
Lung (Inner)	0.26
Lung (Outer)	1.05
Lymph	1.04
Mucous Membrane	1.04
Muscle	1.05
Nail (Finger and Toe)	1.03
Nerve (Spine)	1.04
Pancreas	1.04
Skin/Dermis	1.13
Spleen	1.05
Stomach	1.05
Testis	1.04
Tooth	2.16

Development of the anatomical models of the Sprague–Dawley rat and man used in this paper has been previously described [9], [10]. Briefly, magnetic resonance imaging (MRI) was used to acquire axial scans of the rat. Images of the man were obtained from the Visible Human Project (National Library of Medicine, Bethesda, MD). Initial computer segmentation of tissue types on the man images was completed by CieMed (a collaboration between the National University of Singapore, Singapore, and Johns Hopkins University, Baltimore, MD). The original x, y, z voxel dimensions were 1.0 $\times$ 1.0 $\times$ 1.0 mm for the man and the original MRI x, y, z voxel dimensions for the rat were 0.39 $\times$ 0.39 $\times$ 3.0 mm. Each voxel was color coded and assigned a tissue type. The tissue types and mass density values (g/cm^3) used in the rat and/or man models are shown in Table I.

The permittivity value assigned to a tissue type was calculated based on frequency. These permittivity values were obtained from the four-term Cole–Cole fits published by Gabriel [12]–[15]. For dielectric parameters below 1 kHz, measurement error may affect the dielectric parameters by up to a factor of two [12]. For the higher frequencies investigated in this paper, Table II shows the ratios between the dielectric values or conductivity values measured by Gabriel and other data used as references in [12]. Based on these ratios, we determined the influence on permittivity values on predicted SAR values by processing the rat model at 0.5, 1.0, and 2.0 times the calculated permittivity values (see Table III).

TABLE II
RATIOS BETWEEN DIELECTRIC VALUE (ε) AND CONDUCTIVITY (σ) MEASURED BY GABRIEL [12] AND OTHER DATA USED AS REFERENCES IN [12]. TISSUES SHOWN REPRESENT THOSE WITH THE GREATEST REPRESENTATION IN THE BODY [MAN: MUSCLE (42%), FAT (30%), SKIN (5%), RAT: MUSCLE (45%), FAT (8%), SKIN (11%)]

Frequency (MHz)	Ratio	Muscle		Fat		Skin	
		ε	σ	ε	σ	ε	σ
200	High	1.2	1.45	5	6.60	1	1.6
	Low	0.50	0.45	0.60	0.50	0.6	0.75
500	High	1.2	1.50	3.30	6.40	1	2.6
	Low	0.60	0.80	0.60	0.40	0.6	0.6
2060	High	1.3	1.40	2.50	6.60	1	2.8
	low	0.70	0.45	0.75	0.55	0.8	0.5

TABLE III
PERMITTIVITY VALUES PREDICTED BY THE FOUR-TERM COLE–COLE WERE MULTIPLIED BY 0.5, 1.0, AND 2.0 TO INVESTIGATE HOW THE VARIABILITY IN PERMITIVITY VALUES REPORTED IN THE LITERATURE INFLUENCE THE PREDICTED SAR VALUES IN BIOLOGICAL TISSUE. AS AN EXAMPLE, THE DIELECTRIC (ε) AND CONDUCTIVITY (σ) VALUES FOR MUSCLE AS A FUNCTION OF FREQUENCY AND PERMITTIVITY MULTIPLICATION FACTOR (0.5, 1.0, 2.0) ARE LISTED

Frequency (MHz)	0.5 x		1.0 x		2 x	
	ε	σ	ε	σ	ε	σ
100	32.985	0.3535	65.97	0.707	131.94	1.414
200	30.115	0.3715	60.23	0.743	120.46	1.486
300	29.1	0.385	58.2	0.77	116.4	1.54
400	28.565	0.398	57.13	0.796	114.26	1.592
500	28.225	0.411	56.45	0.822	112.9	1.644
600	27.98	0.425	55.96	0.85	111.92	1.7
700	27.8	0.439	55.6	0.878	111.2	1.756
800	27.6	0.4545	55.2	0.909	110.4	1.818
900	27.5	0.4715	55	0.943	110	1.886
1000	27.4	0.489	54.8	0.978	109.6	1.956
1100	27.3	0.5075	54.6	1.015	109.2	2.03
1200	27.2	0.5275	54.4	1.055	108.8	2.11
1400	27.05	0.571	54.1	1.142	108.2	2.284
1600	26.9	0.6185	53.8	1.237	107.6	2.474
1800	26.75	0.6705	53.5	1.341	107	2.682
2060	26.65	0.727	53.3	1.454	106.6	2.908

To examine the influence of EMF frequency on predicted SAR values, the frequency was varied over a relatively wide range, including that expected to be the resonance frequency according to data in the [3]. The two main limitations on the frequencies examined in this paper were voxel size and computer power. With the FDTD code, voxel size is generally limited to one-tenth the wavelength in tissue. A 1-mm^3 voxel size would thus limit frequencies to less than 10 000 MHz. However, 1-mm^3 voxel size in the man model consists of 414 million voxels, which we predict would require between 12 and 23.6 GB of RAM to process in single and double precision, respectively. Therefore, we utilized man models having larger voxel sizes (3 or 5 mm^3). The 3- and 5-mm^3 man models required 602 and 149 MB of RAM, respectively.

Voxel sizes in the original versions of the anatomical models were stated above. Voxel size was sometimes changed to determine its influence on predicted SAR values or to change the res-

olution of the man model for processing using smaller amounts of RAM. As an example, model resolution was increased in the z-direction by replicating each image slice and decreasing the z dimension of each slice. We realize, of course, that increasing the resolution in this manner does not provide more detailed organ structure, but it does provide a preliminary understanding of the interaction between voxel size and predicted SAR values.

An FDTD program based on a code originally described by Kunz and Leubbers [16] was used to predict localized and whole-body normalized SAR values (W/kg/mW/cm^2). The use of this method is reported in numerous publications each year[1] and has become one of the most frequently used methods to predict SAR values in organic and nonorganic materials. Ongoing research in our laboratory involves comparing the predicted SAR values to those determined empirically using *in vivo* models.

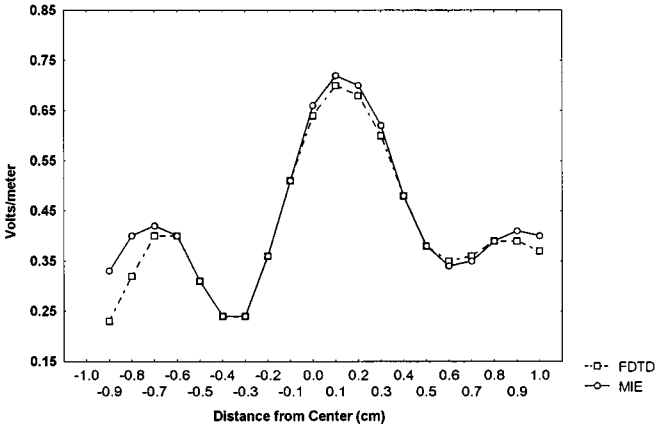

Fig. 1. E-field values (volts per meter) predicted by the FDTD and Mie computational models for a 20-mm-diameter sphere exposed in the far field to 1800 MHz.

A. Model Validation

Spheres were 66 or 105 mm in diameter and composed of material having the dielectric properties of 2/3 muscle. This material was encased in two halves of a Styrofoam shell. The Styrofoam regions in contact with the dielectric material had been coated with epoxy (Bob Smith's Industries, Atascadero, CA). This coating attenuated the amount of water that would be extracted from the dielectric material into the Styrofoam shell during the pre-exposure time period, during which the temperature of the spheres was equilibrating to that of the exposure chamber. Each half was covered with silkscreen and the two halves were held together with tape. A Radiance1 infrared camera system and ImageDesk software (256 $\times$ 256 indium antimonide sensor array sensitive over the 3–5-μm waveband, Amber Engineering Inc., Goleta, CA) were used to record temperature gradients in each half immediately after exposure.

Spheres were placed on a Styrofoam shelf and exposed in the far field to 2060 MHz (L-Band Klyston source, Model 2852, Colber Electronics, Stanford, CT) at a power density of 1.7 W/cm^2. A standard gain horn (26 $\times$ 35 cm, Model 645, Narda, Hauppauge, NY) was used at the end of the waveguide. Incident power density was determined before and after the experiments using a Loral-Narda Electromagnetic Radiation Monitor (Model 8616) with an Isotropic Probe (Model 8623D). To confirm that the probe was isotropic in this application, the average incident power density was determined by making eight separate readings, rotating the probe 45° between each reading. The temperature and humidity of the anechoic chamber (Emerson and Cuming, Canton, MA) were 22 °C and 58%, respectively. Exposure durations for the 66- and 105-mm-diameter spheres were 30 and 60 s, respectively. Data were not corrected for the influence of heat flow after termination of exposure. Data analysis was accomplished using Transform and Plot (Fortner Research, Sterling, VA) and Excel (Microsoft, Redmond, WA) software.

Male Sprague–Dawley rats were obtained from the colonies of Charles River (Wilmington, MA). They were individually housed in standard plastic cages (26 $\times$ 23 $\times$ 20.5 cm) with water available *ad libitum*. Recognizing the influence of body mass on SAR values, all rats used in the validation studies were food restricted and maintained within a weight range of 365–375 g. Rats were fed Formulab 5008 (Purina Meals, St. Louis, MO). The light–dark cycle was 12:12 h (lights on 0700 h) and the room temperature was maintained at 22 °C–23 °C. Rats ($n = 2/\text{orientation}$) were anesthetized and stereotaxically implanted with guide cannulae (Vialon, Becton Dickson, 1.47-mm OD) in the olfactory bulb, hypothalamus, cerebral cortex, and brainstem. The cannulas were held in place with dental acrylic (PlasticOne, Roanoke, VA). The tip of each cannula was plugged so that the temperature probe did not protrude. Prior to EMF exposure, a 1.08-mm OD nonperturbing temperature probe (Model 101, Vitek, Boulder, CO) was placed in each guide cannula. This probe uses carbon impregnated PTFE high-resistance leads to connect to the thick-film thermistor at the probe tip.

All exposures took place in the far field, at a frequency of 2060 MHz (L-Band Klyston source, Model 2852, Colber Electronics, Stanford, CT) and an incident power of 1.0 W/cm^2. Incident power density was measured as described above. The rat was placed on Styrofoam (ledge that was placed 33 cm above carbon-impregnated foam inside an anechoic chamber). The width and height of the ledge was minimized to 5 cm $\times$ 5 cm to reduce perturbations to the field, yet still support the animal's weight. The temperature and humidity inside the chamber were 22 °C–24 °C and 30%–34%, respectively. The local SAR values were determined by making a linear extrapolation from the rate of temperature change during the linear portion of the heating curve using the following relationship:

$$\text{SAR} = (\Delta T \cdot c) \cdot t^{-1} \tag{1}$$

where SAR is in watts per kilogram, T is temperature (°C), t is the time (s) of the sampling period, and c is the specific heat for the tissue of interest. The linear portion of the heating curve corresponded to the first 20 s of exposure and the specific heat of gray matter was used as the tissue of interest [3500 J/°C per kg (17)]. In addition to determining localized SAR, whole-body SAR values ($n = 2/\text{orientation}$) were determined according to the method described by Padilla and Bixby [2].

[1][Online.] Available: http: www.fdtd.org

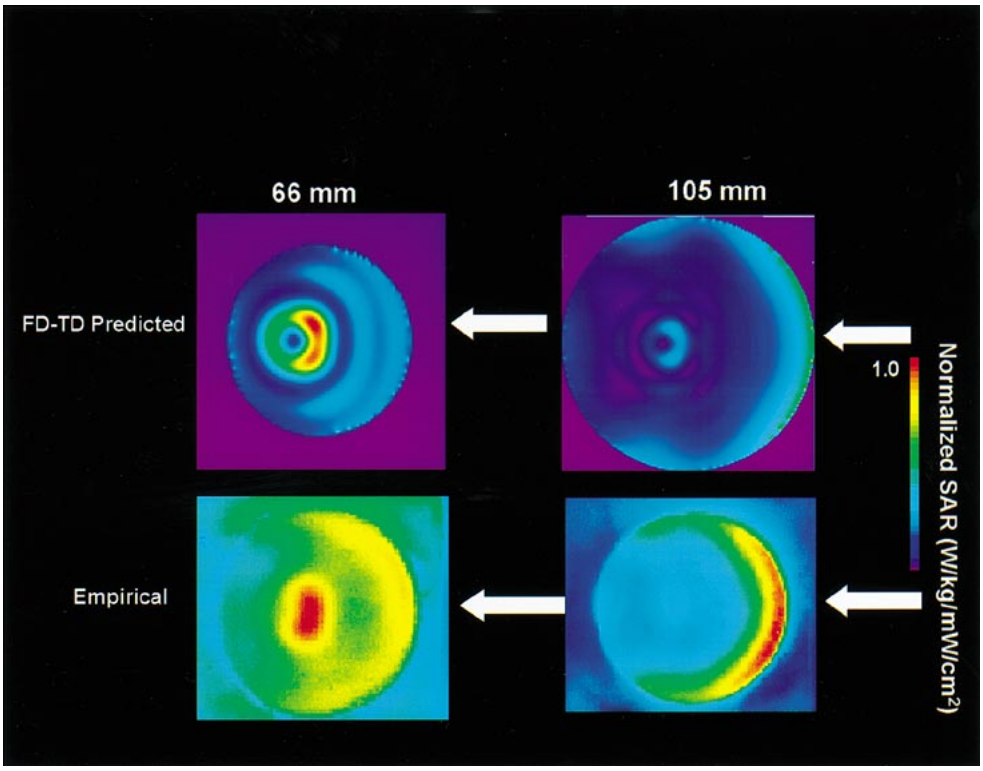

Fig. 2. Top row: distribution of normalized SAR values predicted by the FDTD model for 66- and 105-mm-diameter spheres exposed in the far field to 2060-MHz radiation. The lighter areas represent the higher SAR values. Arrow indicates direction of exposure. Bottom row: temperature gradients recorded by infrared thermography across 66- and 105-mm-diameter spheres after exposure in the far field to 2060-MHz radiation.

III. Results

The FDTD results for the 20-mm-diameter sphere were verified by comparing them with the results from the Mie procedure. Fig. 1 shows the E-field values (volts per meter) predicted by the FDTD and Mie computational models exposed in the far field to 1800 MHz. There is good agreement in the results predicted by the two models.

The FDTD results for the 66- and 105-mm-diameter spheres are shown in Fig. 2. Also shown for comparison purposes are the empirical data as measured by infrared thermography. Normalized SAR values were calculated from these temperature changes and were consistent with those predicted by the FDTD code. The higher SAR values are in the center of the 66-mm sphere and along the leading edge of the 105-mm sphere.

The rat model (334 g as determined by summating mass of all voxels) was processed in the EHK orientation at eight frequencies (300, 400, 500, 600, 700, 900, 1100, and 2060 MHz) (see Fig. 3). The following three vectors comprise electromagnetic fields: the electric field ($\mathbf{E}$), magnetic field ($\mathbf{H}$), and direction of propagation ($\mathbf{K}$). Table IV shows good agreement between the whole-body SAR values calculated for the heterogeneous rat model and those in [3, Fig. 6.16] for a prolate spheroid model of a medium size rat. According to [3, Fig. 6.16], 600 MHz is approximately the resonance frequency for a prolate spheroid model ($\text{volume} = 3.2 \times 10^{-4}$ m^3) of a medium rat (320 g, 20 cm in length). Axial or sagittal sections through our heterogeneous model revealed relatively high SAR values along the ventral surface although the field of propagation was dorsal to ventral.

TABLE IV
NORMALIZED WHOLE-BODY SAR VALUES (W/kg/mW/cm^2) CALCULATED BY FDTD CODE USING THE HETEROGENEOUS MODEL OF THE SPRAGUE–DAWLEY RAT [1.95 × 1.95 × 2.15 mm (x, y, z)] VERSUS THOSE VALUES PREDICTED USING A PROLATE SPHEROID MODEL OF A MEDIUM-SIZE RAT AS GRAPHED IN [3, FIG. 6.16]

Frequency (MHz)	Normalized Whole Body SAR Value (W/kg/mW/cm^2)	
	Heterogeneous Model	RFR Dosimetry Handbook
300	.23	.18
400	.42	.33
500	.95	.60
600	.99	.80
700	.53	.70
900	.46	.50
1100	.46	.24
2060	.36	.14

Permittivity values in the rat model were altered for 500 and 2060 MHz. At 2060 MHz, multiplying all permittivity values by 0.5 increased the whole-body normalized SAR value from 0.36 to 0.41 W/kg/mW/cm^2. Multiplying all permittivity values by 2.0 decreased the whole-body normalized SAR value to 0.31 W/kg/mW/cm^2. This inverse relationship between permittivity and SAR values is consistent with that shown in [3, Fig. 5.7].

Muscle comprised 45% of the rat model and the local normalized SAR value for muscle decreased as the permittivity value increased, which is consistent with the pattern described above for whole-body normalized SAR values. However, the predicted SAR values in some of the other tissues did not follow this pattern. At 2.0× the permittivity value, for example,

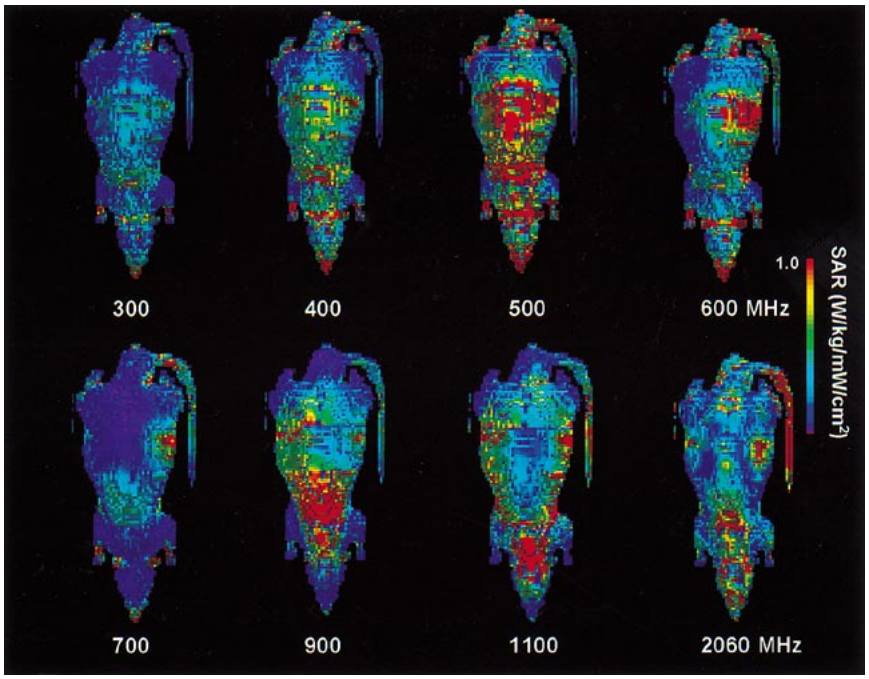

Fig. 3. Calculated normalized SAR values (W/kg/mW/cm^2) in the rat model exposed in the EHK orientation to 300, 400, 500, 600, 700, 900, 1100, and 2060 MHz.

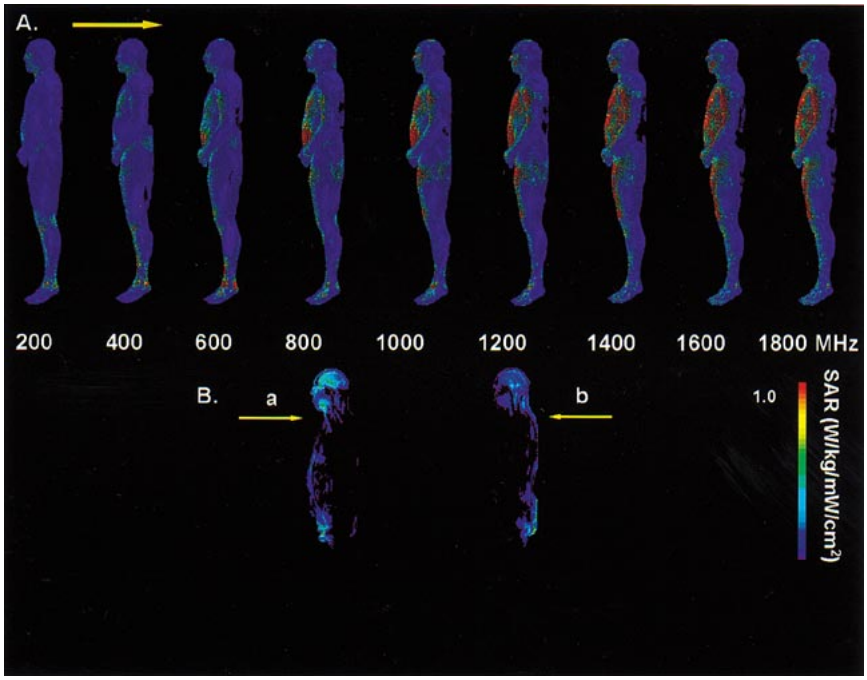

Fig. 4. (a) Calculated normalized SAR values (W/kg/mW/cm^2) in the man model exposed in the EHK orientation to 200, 400, 600, 800, 1000, 1200, 1400, 1600, and 1800 MHz. (b) Sagittal views through the midline of the man model revealing normalized SAR values (W/kg/mW/cm^2) resulting from exposures in the EHK orientation to 800 MHz when the field was propagated in the following directions: a) ventral-to-dorsal and b) dorsal-to-ventral.

the normalized SAR values for ligament were approximately 2.5 times higher than those at 0.5× the permittivity value. Overall, the normalized SAR values were higher for six of the 34 biological tissues when the permittivity values were 2.0× as compared to 0.5×.

The whole-body SAR results at 500 MHz, which is near the resonance frequency for the rat model, were opposite to those observed at 2060 MHz. Multiplying all permittivity values by 0.5 decreased the whole-body normalized SAR value from 0.95 to 0.63 W/kg/mW/cm^2. Multiplying all permittivity values by 2.0 increased the whole-body normalized SAR value to 1.3 W/kg/mW/cm^2. This relationship between permittivity and SAR values is not consistent with that shown in [3, Fig. 5.7]. Overall, the normalized SAR values at 500 MHz were higher for 33 of the 34 biological tissues when the permittivity values were 2.0× as compared to 0.5×.

TABLE V
NORMALIZED WHOLE-BODY SAR VALUES (W/kg/mW/cm^2) CALCULATED BY FDTD CODE USING HETEROGENEOUS MODELS OF THE MAN (3- OR 5-mm^3 VOXELS) EXPOSED IN THE EHK POLARIZATION (WAVE PROPAGATION FROM THE DORSAL-TO-VENTRAL SURFACE OF THE MAN) VERSUS THOSE VALUES PREDICTED USING A PROLATE SPHEROID MODEL OF AN AVERAGE MAN AS GRAPHED IN [3, FIG. 6.3]

Frequency (MHz)	Normalized Whole Body SAR Value (W/kg/mW/cm^2)		
	Heterogeneous Model		RFR Dosimetry Handbook
	3 mm^3	5 mm^3	
70	.270	.290	.25
200	.048	.051	.048
400	.064	.060	.036
600	.067	.066	.034
800	.064	.063	.031
1000	.063	.061	.030
1200	.061	.060	.030
1400	.060	.059	.029
1600	.058	.059	.029
1800	.056	.060	.028
2000	.055	.060	.028

Altering voxel size in the rat model had minor impact on the predicted normalized whole-body SAR values. The rat model was manipulated as described in Section II-A to produce voxel sizes (x, y, z) of either $0.39 \times 0.39 \times 0.43$ mm or $1.95 \times 1.95 \times 2.15$ mm. At 2060 MHz, voxel sizes of approximately 0.4 and 2.0 mm^3 produced SAR values of 0.34 and 0.36 W/kg/mW/cm^2, respectively. The localized SAR values showed similar lackluster differences. Nine of the 34 biological tissues in the high-resolution model had slightly higher SAR values than those in the lower resolution model.

A. Man

The man model was exposed in the EHK orientation to 70, 200, 400, 600, 800, 1000, 1200, 1400, 1600, and 1800 MHz [see Fig. 4(a)]. The highest predicted whole-body SAR value was at 70 MHz, which is consistent with that graphed in [3, Fig. 6.3] (see Table V). Energy absorption was prominent in the regions surrounding the ankles, knees, and neck region for the lower pulse frequencies (200–600 MHz). Increasing the frequency augmented the amount of energy deposited on the skin. Energy absorption within the brain was maximal between 600–800 MHz when the field was propagated in the ventral to dorsal direction. For this determination, the brain SAR value was comprised of data from the gray matter, white matter, and cerebellum. The higher SAR values were throughout the forebrain and midbrain regions. However, when the field was propagated in the dorsal-to-ventral direction, a very different pattern of SAR values was observed in the brain. The higher SAR values were at the interface of the brain, cerebrospinal fluid, and skull toward the base of the brain [see Fig. 4(b)].

The man model was processed at both 3 and 5 mm^3 resolution to determine the effects of voxel size on predicted SAR values. As reported for the rat model, altering voxel size had very little influence on whole-body SAR values (see Table V).

B. Model Validation

Comprehensive development of any model includes its validation by comparison to empirical data. Validation should be accomplished using the actual type of organism used to develop the model. However, with the man model, this is not practical due to ethical concerns regarding the implantation of deep body temperature probes and the scarcity of volunteers. Therefore, validation is accomplished in our laboratory using rats. If there is good correlation between the predicted and empirical results using animal models, that should provide confidence in the data from the man dosimetry model. For the rat, we first compared the normalized whole-body SAR values determined calorimetrically with those predicted by the FDTD code for four exposure orientations (Fig. 5). The calculations of the FDTD code are slightly lower than those determined calorimetrically. However, the relative influence of orientation on whole-body SAR is similar for both methods.

The next level of comparison was between the normalized whole-brain SAR values obtained using the two methods. The rat brain offers an ideal organ for comparison, due to the reliability of stereotaxic probe placements and the ability to easily confirm probe placements in tissue sections following experimentation. The experimentally derived whole-brain SAR values were estimated from the mean SAR of four brain regions at each orientation. The results of this comparison are shown in Fig. 6.

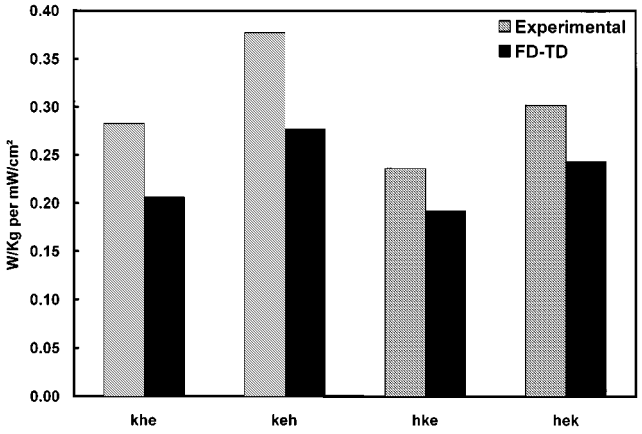

Fig. 5. Comparison of the normalized whole-body SAR values (W/kg/mW/cm^2) determined calorimetrically with the values calculated by FDTD modeling as a function of the rats' orientation in the field.

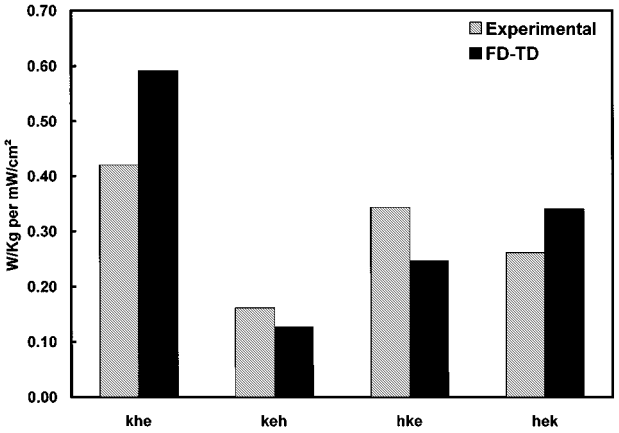

Fig. 6. Comparison between the normalized whole-brain SAR values obtained from experimental methods and the FDTD calculations for four exposure orientations. Values shown are the mean of four brain regions (olfactory bulb, hypothalamus, cerebral cortex, and brainstem) in the rat.

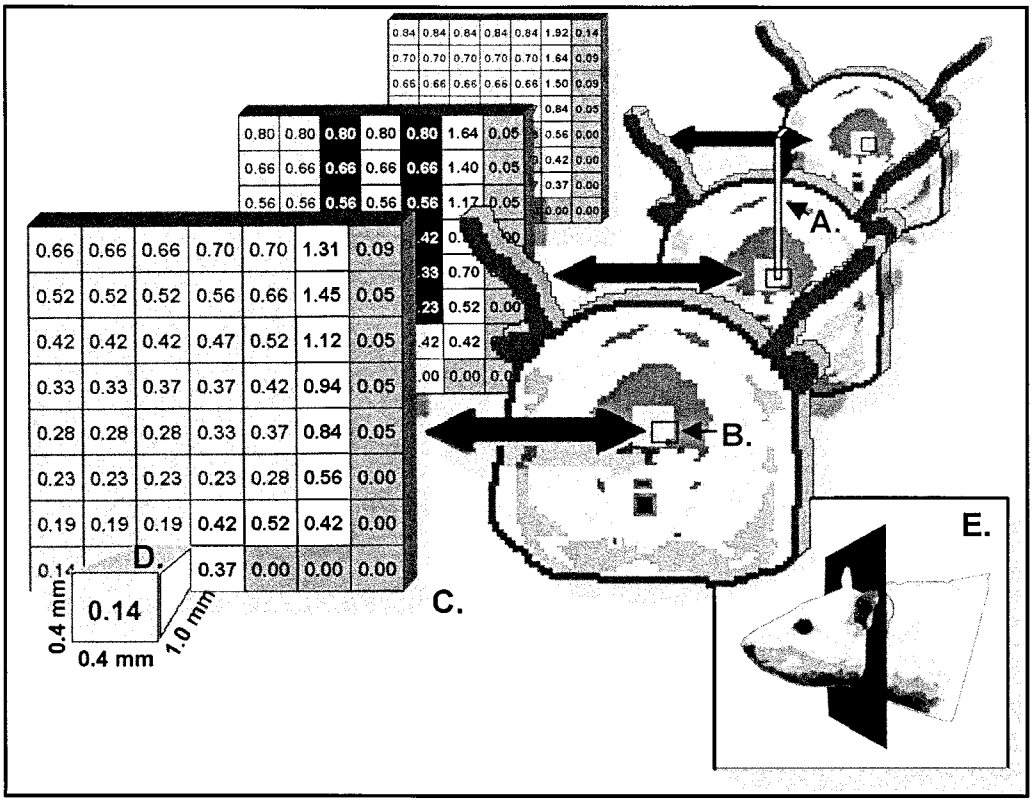

Fig. 7. Schematic diagram illustrating the procedure used to locate the appropriate sampling area. In this example, the area corresponds to the brainstem. The location of each thermal probe was first mapped on: (a) the corresponding anatomical image, as can be seen in the middle slice. The numeric output from the FDTD code was then combined with the graphic image containing the anatomical information. The portion of this procedure corresponding to: (b) the sample area is shown in (c) the table. The sample area for each slice consisted of a 7×7 voxel (x, y) area with the tip of the probe in the center of the area. Each voxel was $0.4 \times 0.4 \times 1.0$ mm (x, y, z) (d). A similar size region was sampled in the adjacent slices, thus the volume of the sample area was 23.5 mm^3 area ($7 \times 7 \times 3$ voxels). (e) The insert contains a picture of a rat head with a plane through the head corresponding to the location of the slices.

The agreement between the two methods is good and certainly within the error of the experimental method. The greater value for the FDTD calculation, compared with the experimental estimation, in the khe orientation, is discussed below.

In order to compare the regional SAR values obtained experimentally with those from FDTD calculations, the SAR value for each voxel must be linked to its anatomical location. The process is described in detail in Fig. 7. The spatial resolution of the FDTD output is much greater than the volume that the thermal probe is capable of resolving. For comparison between the two methods, an average SAR value was obtained by calculating the mean of a 23.5 mm^3 volume ($7 \times 7 \times 3$ voxels). This sample size was chosen because it was the smallest uniform three-dimensional volume that encompassed the thermal probe (i.e., x: 7 voxels $\cdot$ 0.4 mm $=$ 2.8 mm; y: 7 voxels $\cdot$ 0.4 mm $=$ 2.8 mm; z: 3 voxels $\cdot$ 1.0 mm $=$ 3.0 mm).

For most cases, there was a good match between experimentally estimated and FDTD calculated SAR values for the four brain regions. A comparison of the influence of orientation on the SAR in the brainstem is shown in Fig. 8. Overall, the results of comparing SAR values across regions for a given orientation show a reasonable agreement between methods. As would be expected, the match was closest when the sampling volume around the temperature probe contains uniform SAR values that were close to the whole-body SAR value. Mismatches between methods occurred when the FDTD code calculated relatively high or low SAR values. In these cases, the extremes in SAR values were not reflected in the thermal data (i.e., high and low FDTD SAR values corresponded to underestimation or overestimation of experimentally estimated SAR values, respectively).

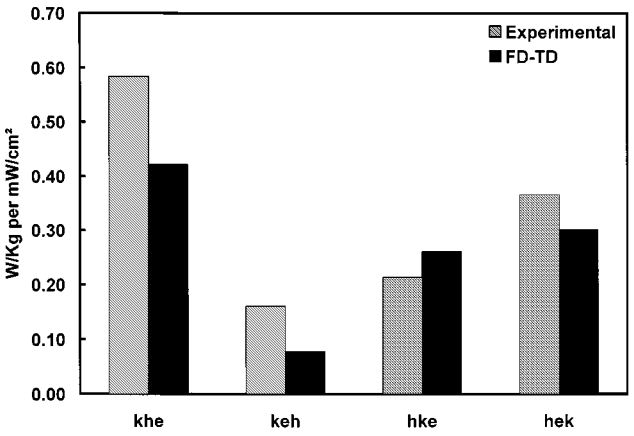

Fig. 8. Comparison between experimentally and FDTD determined SAR values (W/kg/mW/cm^2) in the brainstem of the rat as a function of orientation in the field.

IV. Discussion

Orientation, relative to the EMF source, has a profound influence on regional SAR values and must be accounted for in order

to interpret bioeffects data. As a practical matter, however, it is not possible to empirically determine the regional SAR values for all experimental conditions of interest. Recently, though, the use of computer codes and heterogeneous anatomical models has vastly increased our knowledge about how energy is absorbed during EMF exposure. Extremely complicated patterns of energy absorption have been revealed that would be difficult, if not impossible, to predict by extrapolating data from localized temperature measurements.

Comparing localized SAR values determined experimentally via well-established thermal models with those obtained using the FDTD method demonstrate good agreement, except when the FDTD method calculates "hot or cold" spots (relative to whole-body average SAR). In these cases, the disparity is at least partially due to confounding factors in the thermal method caused by thermal loss or gain from surrounding regions with dissimilar SAR values [18]. This complication emphasizes the fact that SAR alone may not provide an adequate description of the regional thermal environment. Furthermore, present models usually do not take into account the role of thermoregulatory components (e.g., conduction, convection, and blood flow) in determining the increase in temperature occurring in a specific body region during EMF exposure. Future computer models will, therefore, need to account for the influence of such components [19]–[22].

In summary, the effects of simultaneously altering all tissue permittivity values on whole-body and localized SAR values were determined in this paper. We have recently initiated studies to determine the effects of varying the permittivity value for a single tissue type on the SAR values for that organ and the immediately surrounding organs. In addition to this parameter, we are also beginning to determine the effects of multiple-frequency exposures on SAR values; such multiple-frequency exposures might be experienced by individuals while conducting measurements on antenna arrays and are, thus, of profound interests in terms of human exposure issues.

ACKNOWLEDGMENT

The authors gratefully acknowledge and appreciate the graphical and technical assistance of J. Belcher, B. Brewer, J. Esquivel, E. Foster, M. Gilbert, P. Gonzales, D. Hatcher, P. Henry, D. Jentsch, D. Lane, G. Lantrip, K. Mylacraine, K. Obenshain, L. A. Paulus, R. Post, J. Roe, J. Villacis, and K. Watt, and the animal care by G. Lantrip.

The animals involved in this study were procured, maintained, and used in accordance with the Federal Animal Welfare Act and the *Guide for the Care and Use of Laboratory Animals*, prepared by the Institute of Laboratory Animal Resources, National Research Council. Trade names of materials and/or products of commercial or nongovernmental organizations are cited as needed for precision. These citations do not constitute official endorsement or approval of the use of such commercial materials and/or products.

REFERENCES

[1] E. L. Hunt and R. D. Phillips, "Absolute physical dosimetry for whole animal experiments," in *Joint U.S. Army/Georgia Inst. Technol. Microwave Dosimetry Workshop Dig.*, Washington, DC, 1972, pp. 74–77.

[2] J. P. Padilla and R. Bixby, "Using Dewar–Flask calorimetry and rectal temperatures to determine the specific absorption rates of small rodents," USAF School Aerospace Med., Brooks AFB, TX, USAFSAM-TR-86-3, 1986.

[3] C. H. Durney, H. Massoudi, and M. F. Iskander, "Radiofrequency radiation dosimetry handbook," USAF School Aerospace Med., Brooks AFB, TX, USAFSAM-TR-85-73, 1986.

[4] A. W. Guy, M. D. Webb, and C. C. Sorensen, "Determination of power absorption in man exposed to high frequency electromagnetic fields by thermographic measurements on scale models," *IEEE Trans. Biomed. Eng.*, vol. BME-23, pp. 361–371, Sept. 1976.

[5] T. W. Dawson, K. Caputa, and M. A. Stuchly, "Influence of human model resolution on computed currents induced in organs by 60-Hz magnetic fields," *Bioelectromagnetics*, vol. 18, pp. 478–490, 1997.

[6] P. J. Dimbylow, "FDTD calculations of the whole-body averaged SAR in an anatomically realistic voxel model of the human body from 1 MHz to 1 GHz," *Phys. Med. Biol.*, vol. 42, pp. 479–490, 1997.

[7] C. M. Furse and O. P. Gandhi, "Calculation of electric fields and currents induced in a millimeter-resolution human model at 60 Hz using the FDTD method," *Bioelectromagnetics*, vol. 19, pp. 293–299, 1998.

[8] G. D. Lapin and C. Allen, "Requirements for accurate anatomical imaging of the rat for electromagnetic modeling," in *Proc. 19th Int. IEEE/EMBS Conf.*, Chicago, IL, 1997, pp. 2480–2483.

[9] P. A. Mason, T. J. Walters, J. W. Fanton, D. N. Erwin, J.-H. Gao, J. W. Roby, J. L. Kane, K. A. Lott, L. E. Lott, and R. V. Blystone, "Database created from magnetic resonance images of a Sprague–Dawley rat, rhesus monkey, and pigmy goat," *Fed. Amer. Soc. Exper. Biol. J*, vol. 9, pp. 434–440, 1995.

[10] P. A. Mason, J. M. Ziriax, W. D. Hurt, T. J. Walters, K. L. Ryan, D. A. Nelson, K. I. Smith, and J. A. D'Andrea, "Recent advancements in dosimetry measurements and modeling," in *Radio Frequency Radiation Dosimetry*, B. J. Klauenberg and D. Miklavcic, Eds. Norwell, MA: Kluwer, 2000, pp. 141–155.

[11] W. D. Hurt, J. M. Ziriax, and P. A. Mason, "Variability in EMF permittivity values: Implications for SAR calculations," *IEEE Trans. Biomed Eng.*, vol. 47, pp. 396–401, Mar. 2000.

[12] C. Gabriel, "Compilation of the dielectric properties of body tissue at RF and microwave frequencies," USAF School Aerospace Med., Brooks AFB, TX, AL/OE-TR-1996-0037, 1996.

[13] C. Gabriel, S. Gabriel, and E. Corthout, "The dielectric properties of biological tissues: I. Literature survey," *Phys. Med. Biol.*, vol. 41, pp. 2231–2249, 1996.

[14] S. Gabriel, R. W. Lau, and C. Gabriel, "The dielectric properties of biological tissues: II. Measurement in the frequency range 10 Hz to 20 GHz," *Phys. Med. Biol.*, vol. 41, pp. 2251–2269, 1996.

[15] S. Gabriel, R. W. Lau, and C. Gabriel, "The dielectric properties of biological tissues: III. Parametric models for the dielectric spectrum of tissues," *Phys. Med. Biol.*, vol. 41, pp. 2271–2293, 1996.

[16] K. S. Kunz and R. J. Luebbers, *The Finite Difference Time Domain Method for Electromagnetics*. Boca Raton, FL: CRC Press, 1993.

[17] R. W. Olsen, "Temperature distributions during induced deep hypothermia and subsequent circulatory arrest: An experimental and numerical study," Ph.D. dissertation, Grad. School Biomed. Sci., Univ. Texas Health Sci. Center, Dallas, TX, 1985.

[18] E. G. Moros and W. F. Pickard, "On the assumption of negligible heat diffusion during the thermal measurement of a nonuniform specific absorption rate," *Radiat. Res.*, vol. 152, pp. 312–320, 1999.

[19] K. R. Foster, A. Lozano-Nieto, and P. J. Riu, "Heating of tissues by microwaves: Model analysis," *Bioelectromagnetics*, vol. 19, pp. 420–428, 1998.

[20] D. A. Nelson, M. T. Nelson, T. J. Walters, and P. A. Mason, "Skin heating of millimeter wave irradiation—Thermal modeling results," *IEEE Trans. Microwave Theory Tech.*, vol. 48, pp. 2111–2120, Nov. 2000.

[21] T. J. Walters, P. A. Mason, K. L. Ryan, D. A. Nelson, and W. D. Hurt, "A comparison of SAR values determined empirically and by FD-TD modeling," in *Radio Frequency Radiation Dosimetry*. Norwell, MA: Kluwer, 2000, pp. 207–216.

[22] T. J. Walters, D. W. Blick, L. R. Johnson, E. R. Adair, and K. R. Foster, "Heating and pain sensation produced in human skin by millimeter waves: Comparison to a simple thermal model," *Health Phys.*, vol. 78, pp. 259–267, 2000.

Patrick A. Mason, photograph and biography not available at time of publication.

William D. Hurt (SM'78), photograph and biography not available at time of publication.

Thomas J. Walters, photograph and biography not available at time of publication.

John A. D'Andrea (M'81), photograph and biography not available at time of publication.

Peter Gajšek, photograph and biography not available at time of publication.

Kathy L. Ryan, photograph and biography not available at time of publication.

David A. Nelson, photograph and biography not available at time of publication.

Kristen I. Smith, photograph and biography not available at time of publication.

John M. Ziriax, photograph and biography not available at time of publication.